Energy & Environmental Science

PAPER

View Article Online
View Journal | View Issue

Cite this: *Energy Environ. Sci.*, 2017, **10**, 2570

Efficacious engineering on charge extraction for realizing highly efficient perovskite solar cells†

Shizhong Yue, [ab] Kong Liu, [ab] Rui Xu, [c] Meicheng Li, [d] Muhammad Azam, [ab] Kuankuan Ren, [ab] Jun Liu, [ab] Yang Sun, [ab] Zhijie Wang, *[ab] Dawei Cao, [e] Xiaohong Yan, [e] Shengchun Qu, *[ab] Yong Lei *[c] and Zhanguo Wang [ab]

Received 19th September 2017,
Accepted 13th November 2017

DOI: 10.1039/c7ee02685d

rsc.li/ees

Efficient extraction of photogenerated charge carriers is of significance for acquiring a high efficiency for perovskite solar cells. In this paper, a systematic strategy for effectively engineering the charge extraction in inverted structured perovskite solar cells based on methylammonium lead halide perovskite ($CH_3NH_3PbI_{3-x}Cl_x$) is presented. Intentionally doping the chlorine element into the perovskite structure is helpful for obtaining a high open circuit voltage. The engineering is carried out by modifying the aluminium cathode with zirconium acetylacetonate, doping the hole transport layer of nickel oxide (NiO_x) with copper and using an advanced fluorine doped tin oxide (FTO) substrate. This improves the bandgap alignment of the whole device, and thus, is of great benefit for extracting the charge carriers by promoting the transport rate and reducing the trap states. Consequently, an optimized power conversion efficiency of 20.5% is realized. Insights into how to extract charge carriers efficiently with a minimum energy loss are discussed.

Broader context

Recently, organic–inorganic hybrid perovskite materials have attracted unprecedented attention for cost-effective fabrication of highly efficient photovoltaic devices. The power conversion efficiency has experienced a rapid evolution from 3% to over 20% within eight years. In the construction of the efficient perovskite solar cells, the active material is usually sandwiched in multiple layers to form a typical P–I–N configuration. The key factors governing the extraction of the charge carriers are the bandgap alignment across the whole device and the conducting nature of each component. Although tremendous efforts have been focused on this issue by proposing large varieties of materials as the charge transport layers or buffer layers, each design focuses on the improvement of one aspect and seems to lack a systematic consideration. In this paper, a systematic strategy is provided for effectively engineering the charge extraction in an inverted structure of perovskite solar cells based on $CH_3NH_3PbI_{3-x}Cl_x$. The engineering was carried out using a full optimization of the cathode, electron transport layers, active layer, hole transport layer and the anode. An optimized power conversion efficiency of 20.5% was realized, which could be the largest value for a $CH_3NH_3PbI_{3-x}Cl_x$-based device. Thus, insights on how to efficiently manage the extraction of charge carriers are demonstrated.

Introduction

Recently, organic–inorganic hybrid perovskite materials have emerged as an impressive model for fabricating highly efficient solar cells. Such a series of materials presents tunable bandgap values, a high absorption coefficient, a long lifetime of charge carriers and high charge mobility.[1–3] An attractive power conversion efficiency (PCE) of over 20% has been reported.[3,4] In the construction of perovskite solar cells (PVSCs), the active material is usually sandwiched by multiple layers to form a typical P–I–N configuration. The purposely designed built-in potential across the device is energetically favorable for separating excitons and capturing charge carriers by the electrodes.

The quality of the perovskite film plays a key role in the device performance, and tremendous efforts have been taken in order to acquire a good film for highly efficient photovoltaic devices.[4–6] The film quality has been intensively optimized, and thus, the extent to which the PCE can be further improved by quality optimization of the perovskite film is limited. However, the qualities

[a] *Key Laboratory of Semiconductor Materials Science, Beijing Key Laboratory of Low Dimensional Semiconductor Materials and Devices, Institute of Semiconductors, Chinese Academy of Sciences, Beijing, 100083, People's Republic of China. E-mail: wangzj@semi.ac.cn, qsc@semi.ac.cn*

[b] *College of Materials Science and Opto-Electronic Technology, University of Chinese Academy of Sciences, Beijing 100049, China*

[c] *Institut für Physik & IMN MacroNano® (ZIK), Technische Universität Ilmenau, 98693 Ilmenau, Germany. E-mail: yong.lei@tu-ilmenau.de*

[d] *State Key Laboratory of Alternate Electrical Power System with Renewable Energy Sources, North China Electric Power University, Beijing, 102206, China*

[e] *Department of Physics, Faculty of Science, Jiangsu University, Zhenjiang 212013, China*

† Electronic supplementary information (ESI) available. See DOI: 10.1039/c7ee02685d

of the charge transport layers and the electrodes are also of great significance and this topic deserves some extensive research attention.[7] A series of materials has been proposed to construct an effective P–I–N configuration with the perovskite film, including p-type semiconductors and polymers (*e.g.*, nickel(II) oxide (NiO) and PTAA) for hole transport layers,[8,9] n-type semiconductors (*e.g.*, titanium oxide and zinc oxide) and organic semiconductors {*e.g.*, [6,6]-phenyl C_{61}butyric acid methyl ester ($PC_{61}BM$)} for electron transport layers,[10–12] organic molecules (poly [(9,9-bis(3′-(*N*,*N*-dimethylamino)propyl)-2,7-fluorene)-*alt*-2,7-(9,9-dioctylfluorene)] (PFN), BCP) as the buffer layer to enhance the charge transport to the anode or cathode.[13,14] However, the large varieties of these methodologies and materials seem to lack systematic consideration and a device design principle is needed to further enhance the device outcomes.

In this paper, a systematic strategy is provided for the construction of highly efficient PVSCs from the point of view of effective extraction of photogenerated charge carriers. The engineering is carried out using three steps. Firstly, an efficacious method was chosen to modify the aluminium (Al) cathode using zirconium acetylacetonate (ZrAcac). Such a molecule is beneficial for extracting electrons to the cathode by promoting the electron transport and reducing the corresponding trap states. Then the hole extracting capability of the nickel oxide (NiO_x) layer is optimized using a copper (Cu) dopant. This could improve the bandgap alignment of the device, thus the transport of holes here is obviously boosted with a minimum energy loss. To reduce the conductivity loss of the anode resulting from the annealing procedure of the NiO_x film, a highly conductive fluorine doped tin oxide (FTO) substrate was used. An optimized power conversion efficiency of 20.5% is realized, which could, so far, be the largest value ever obtained for the methylammonium lead halide perovskite ($CH_3NH_3PbI_{3-x}Cl_x$)-based device. The configuration principle for perovskite photovoltaic devices is given in a systematic way.

Results and discussion

Fig. 1a shows the schematic structure of the perovskite photovoltaic devices with a typical inverted structure. The perovskite film is sandwiched by NiO_x and $PC_{61}BM$ to form a P–I–N planar architecture, where the holes and electrons are designed to be transported to the electrodes through NiO_x and $PC_{61}BM$/ZrAcac, respectively. The corresponding cross-sectional scanning electron microscopy (SEM) image of the structure is given in Fig. 1b, where the clear multi-layered structure can be observed. The thickness of the $CH_3NH_3PbI_{3-x}Cl_x$ is measured as 280 nm, which is sufficient for absorbing the sunlight efficiently.

The perovskite film in the device was prepared using a standard one-step method with a subsequent solvent treatment procedure using toluene.[15] Fig. 1c displays the X-ray diffraction (XRD) pattern of the as-grown film on the ITO substrate (red curve). The series of diffraction peaks at 14°, 20.5°, 28°, and 41° corresponds to the standard diffraction from (110), (112), (220) and (224) crystal planes of $CH_3NH_3PbI_{3-x}Cl_x$, respectively.[15] Diffraction peaks of lead chloride ($PbCl_2$) were not observable and only a slight peak from lead iodide (PbI_2) can be seen. Considering the absence of PbI_2 in the film without chlorine addition (blue curve), this result indicates that the chlorine is

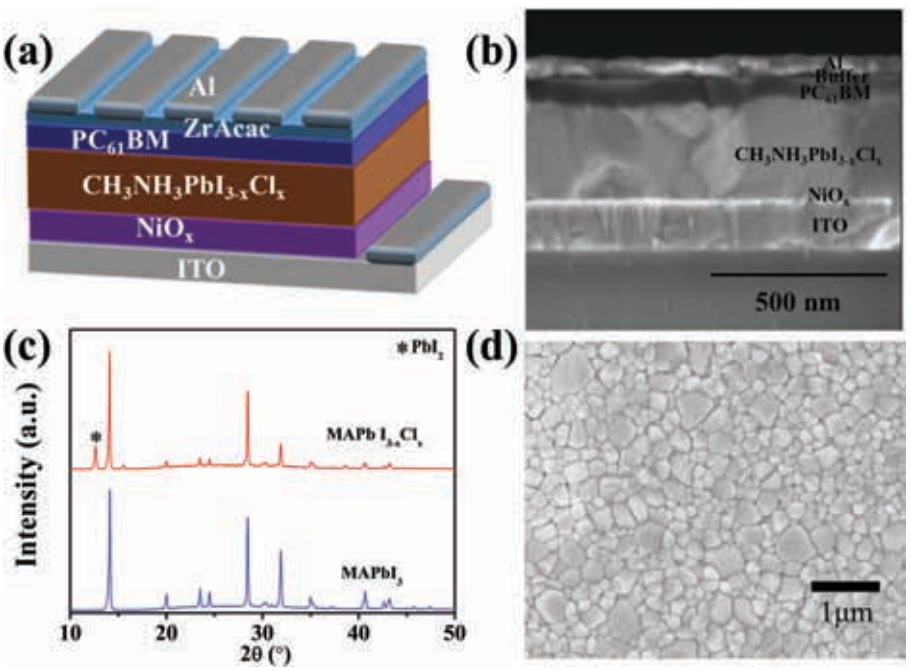

Fig. 1 (a) The schematic structure of the perovskite photovoltaic device. (b) The cross-sectional scanning electron microscopy (SEM) image of the perovskite photovoltaic devices. (c) X-ray diffraction patterns of the different perovskite films on an indium tin oxide (ITO) substrate. (d) Top view SEM image of the perovskite film on ITO/NiO_x.

incorporated or doped to the perovskite structure with the iodine element not being consumed well, thus leaving a tiny amount of PbI_2. The tiny amount of PbI_2 has been proven to have a somewhat positive effect on the device performance (*e.g.*, reducing the ionic defect migrations and enhancing the lifetime of the charge carriers).[16–18] The X-ray photoelectron spectrum (XPS) of the material in Fig. S1 (ESI†) also demonstrates that the material has an acceptable purity without other elemental contaminants. The stoichiometry of this film was determined using the resolved XPS spectra and the results are shown in ESI† (Fig. S1a) and discussed in Section S1 of the ESI.† The top view SEM image of the perovskite film is shown in Fig. 1d, where the size of the perovskite crystal could be measured to be 100–500 nm and no obvious pinholes were discerned. In addition, the absorption spectra given in Fig. S3 (ESI†) indicate a bandgap value of 1.62 eV for the $CH_3NH_3PbI_{3-x}Cl_x$ film, which is 0.04 eV larger than the film prepared without chlorine (Cl) doping. The ultraviolet photoelectron spectrum (UPS) of the Cl doped film shown in Fig. S3c (ESI†) yields a valence band position of 5.82 eV and a Fermi level of 4.70 eV. These results suggest that the film already shows potential for use in highly efficient photovoltaic devices from the aspects of morphology and material.

In order to capture the photogenerated electrons in the perovskite film efficiently, a thin layer of ZrAcac was purposely inserted between the $PC_{61}BM$ and Al cathode. The Fourier infrared and Raman spectra of the ZrAcac film (Fig. S4a; ESI†) show the specific molecular feature of ZrAcac and the corresponding XRD spectrum (Fig. S4b; ESI†) does not demonstrate the presence of zirconium dioxide (ZrO_2), indicating the stability of the molecule in the device. Fig. 2a shows the transient photoluminescence (PL) curves of structures based on ITO/$CH_3NH_3PbI_{3-x}Cl_x$/$PC_{61}BM$ and ITO/$CH_3NH_3PbI_{3-x}Cl_x$/$PC_{61}BM$/ZrAcac. Overall, the PL signals of the two structures present a fast decay, indicating a fast charge dissociation and collection.[19] It is worth noting that the structure with the buffer layer presents a faster decay than the one without it. Considering that the buffer layer is for modifying the electron transport from $PC_{61}BM$ to Al, this result demonstrates that the presence of ZrAcac could promote the transport of electrons to the cathode by reducing the possibility of recombination. The current density *versus* voltage (*J*–*V*) curves of the series of devices with various modifications on electron transport are given in Fig. 2b. The corresponding PCE statistical values are given in Fig. S5 (ESI†) and Table 1.

The reference device without any modification delivers a short-circuit current density (J_{sc}) of 21.98 mA cm^{-2}, an open-circuit voltage (V_{oc}) of 1.08 V, fill factor (FF) of 55.48% and PCE of 13.17%. This result is comparable to previously reported values.[20] To check the modification effect of ZrAcac, the films were spin-coated with different concentrations of the ethanol stock solutions. As shown in Fig. 2b, with the increase of the concentration from 1 to 2 mg mL^{-1}, the device shows an increasing in PCE and outperforms the bare device. This indicates that the presence of ZrAcac does indeed boost the device efficiency, but the film could not be too thick because of the insulating nature of ZrAcac. As the film thickness was further increased by enhancing the concentration of the stock solution, the efficiency drops, particularly in relation to FF. These results suggest that the functionality of ZrAcac is similar to that of PFN in polymer solar cells and the positive

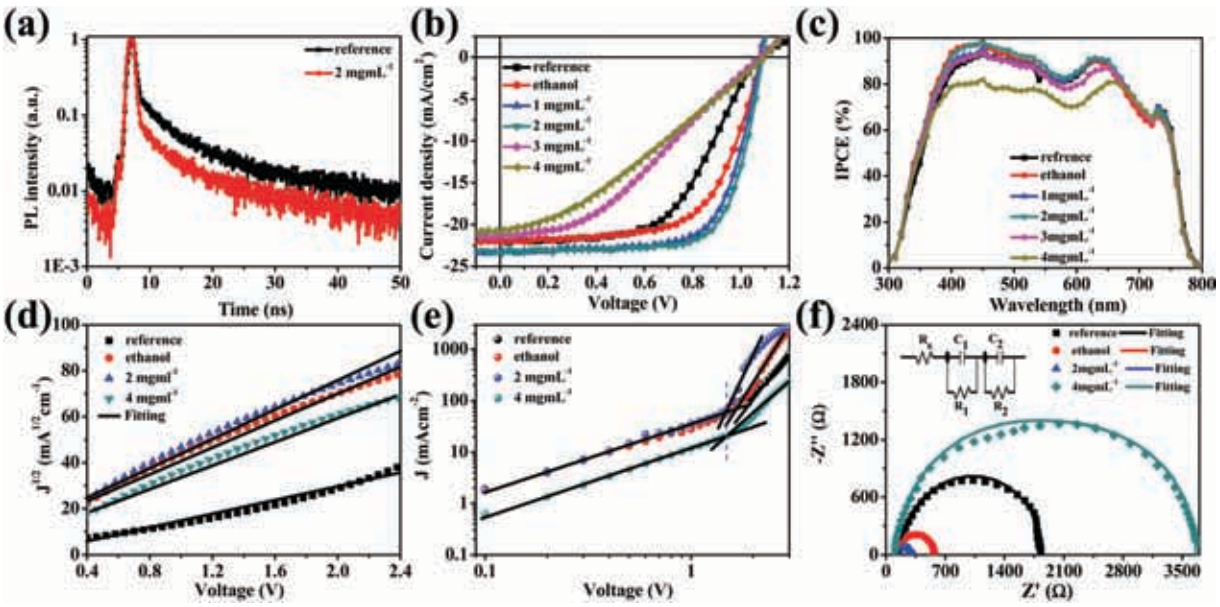

Fig. 2 (a) PL decay curves of the devices with a structure of ITO/$CH_3NH_3PbI_{3-x}Cl_x$/$PC_{61}BM$ (with and without ZrAcac). (b) The curves of current density *versus* voltage (*J*–*V*) of devices with different concentrations of stock solution for spin-coating the ZrAcac buffer layer. The curves were measured under standard solar simulated light illumination (AM 1.5). (c) The IPCE spectra of the corresponding devices. (d) $J^{1/2}$–*V* curves of the electron only devices with the structure of ITO/Al/$PC_{61}BM$ (or modified by ZrAcac)/Al. (e) *J*–*V* curves of the electron only devices with the structure of ITO/Al/$CH_3NH_3PbI_{3-x}Cl_x$/$PC_{61}BM$ (or modified by ZrAcac)/Al. (f) Nyquist plots of the devices in (b) measured in the dark at $V \approx V_{oc}$ (the left inset is the equivalent circuit model).

Table 1 The photovoltaic performance of the perovskite solar cells shown in Fig. 2b

Samples	J_{sc} (mA cm^{-2})	V_{oc} (V)	FF (%)	PCE (%)
Reference	22.50 ± 0.42	1.07 ± 0.01	55.56 ± 1.32	13.38 ± 0.36
Ethanol	22.34 ± 0.31	1.08 ± 0.01	63.66 ± 1.62	15.29 ± 0.48
1 mg mL^{-1}	22.31 ± 1.12	1.08 ± 0.01	70.28 ± 3.39	16.90 ± 0.42
2 mg mL^{-1}	23.53 ± 0.32	1.10 ± 0.01	70.04 ± 1.47	18.05 ± 0.58
3 mg mL^{-1}	22.56 ± 0.36	1.08 ± 0.01	40.18 ± 1.90	9.76 ± 0.36
4 mg mL^{-1}	21.59 ± 1.13	1.08 ± 0.01	35.18 ± 1.10	8.21 ± 0.44

contribution to the device performance is interface modification to reduce the electron trapping possibilities between $PC_{61}BM$ and Al.[13] It is also worth noting that the device was also fabricated by using an ethanol treatment on the $PC_{61}BM$ film before Al deposition to check the effectiveness of ZrAcac. Although the corresponding device outperforms the reference device, this was attributed to the fact that ethanol could boost the crystallinity of the $PC_{61}BM$ film and improve the corresponding electron conductivity,[21,22] and the device still delivers a lower PCE in comparison with the outperformed device in Table 1 with 2 mg mL^{-1} ZrAcac modification (PCE 18.6%). To obtain more information, the incident photon-to-current efficiency (IPCE) spectra of the series of devices were measured and the results are shown in Fig. 2c. All the spectra exhibit a broad spectrum of converting photon energy into current in the range of 300-800 nm, and this is consistent with the absorption spectrum shown in Fig. S3a (ESI†). The high values of IPCE indicate a good capability for converting solar energy to electricity for the devices fabricated in this research. The integrated J_{sc} values obtained from the IPCE spectra are shown in Fig. S6 (ESI†) and these values approximately agree with those from the *J–V* curves, although they are slightly lower than the value from *J–V* curve. The lower value phenomenon results from the fact the *J–V* curves were measured in a glove box whereas the IPCE spectra were obtained under ambient conditions. Because the perovskite solar cells are sensitive to the humidity in the air, such a slightly lowered integrated photocurrent value is reasonable.

Using the space charge limited current method on the electron only device structure, the electron mobility of the devices with different modifications at the interface of $PC_{61}BM$ and Al was investigated. Fig. 2d shows that the $J^{1/2}$–*V* curves of the series of electron only devices (ITO/Al/$PC_{61}BM$ (or modified $PC_{61}BM$)/Al) fitted with the Mott–Gurney law.[23] The device fabricated with 2 mg mL^{-1} ZrAcac solution, as expected, presented the largest electron mobility, 4.20×10^{-4} cm^2 V^{-1} s^{-1}, which is almost 4-fold higher than the device without modification. Either a lower or higher concentration than 2 mg mL^{-1} would induce a deterioration in electron mobility. This is consistent with the performance parameters of the full devices, indicating that the presence of ZrAcac with an appropriate thickness does indeed facilitate the electron transport of the device. More details on the $J^{1/2}$–*V* curves in a large voltage range and on the corresponding fitted curves using the Mott-Gurney law are given in Fig. S7 (ESI†). In addition, the electron trap-state density of the electron only devices (ITO/Al/$CH_3NH_3PbI_{3-x}Cl_x$/$PC_{61}BM$ (or modified $PC_{61}BM$)/Al) were also measured. Fig. 2e shows the *J–V* curves of the corresponding devices. The linear relationship indicates an Ohmic response of the electron only devices at a low bias voltage. When the voltage goes beyond the kink point, the current quickly increases nonlinearly, demonstrating that the trap-states are completely filled. The trap-state density can be calculated using the equation:[24]

$$V_{TFL} = \frac{en_t L^2}{2\varepsilon\varepsilon_0} \quad (1)$$

where V_{TFL} is the trap-filled limit voltage, e is the elementary charge of the electron, L is the perovskite film thickness, ε is the relative dielectric constant of $CH_3NH_3PbI_{3-x}Cl_x$ (ε = 28.8), ε_0 is the vacuum permittivity, and n_t is the trap-state density. The V_{TFL} values in different devices are listed in Table S1 (ESI†). The values for the density of trap states are also included. In comparison with the reference device, the modified device presents an obvious decrease in electron trap-state density and this supports the analysis described previously. To directly obtain the charge transport information of the devices, the impedance spectra were measured. As shown in Fig. 2f, in comparison with the reference device, the modified devices present a decline in the diameter of the curves as the concentration of ZrAcac stock solution increases from 0 to 2 mg mL^{-1} and the diameter increases as the concentration is further increased to 4 mg mL^{-1}. Considering that the diameter is inversely proportional to the charge transport resistance, this result illustrates that a suitable thickness of ZrAcac is helpful for reducing the charge transport resistance of the device. Using the equivalent circuit as shown in the inset of Fig. 2f, the detailed parameters for charge transport are given in Table S2 (ESI†).

Next, the hole transport of the device was optimized. Although the use of Cu doped NiO_x thin film has been reported as the hole transport layer in PVSCs,[25,26] systemically tuning the hole conducting properties of this layer has not received much attention. The doping was performed by mixing a tiny amount of $Cu(ac)_2$ with the $Ni(ac)_2$ precursor for spin-coating the film, before annealing at 340 °C for 1 h. Fig. S8 (ESI†) shows the XRD patterns of the resulting NiO_x and 5% Cu doped NiO_x films. Both patterns present a series of diffraction peaks at 37°, 43° and 62° corresponding to the standard diffraction from the (111), (200) and (220) crystal planes of NiO,[27] respectively. Synthetic Ni diffraction peaks could also be observed from the two patterns, and this was consistent with a previously reported observation.[28] In addition, the 5% Cu doped film exhibits a series of diffraction peaks from copper(II) oxide (CuO) and copper(I) oxide Cu_2O, although the intensity is low because of the tiny amount used for doping. This indicates the presence of Cu related oxides in the NiO_x film. The XPS spectrum of the 5% Cu doped NiO_x film, as shown in Fig. S9a (ESI†), also demonstrates the presence of copper oxide (CuO_x) in the NiO_x film. Additionally, resolved Ni 2p peaks are shown in Fig. S9b (ESI†) and the characteristic features including the multiplet split are in agreement with those found in the literature.[29] As shown in Fig. S9c (ESI†), the Cu 2p peaks are resolved and peaks at 932.5 eV and 952.6 eV correspond to the

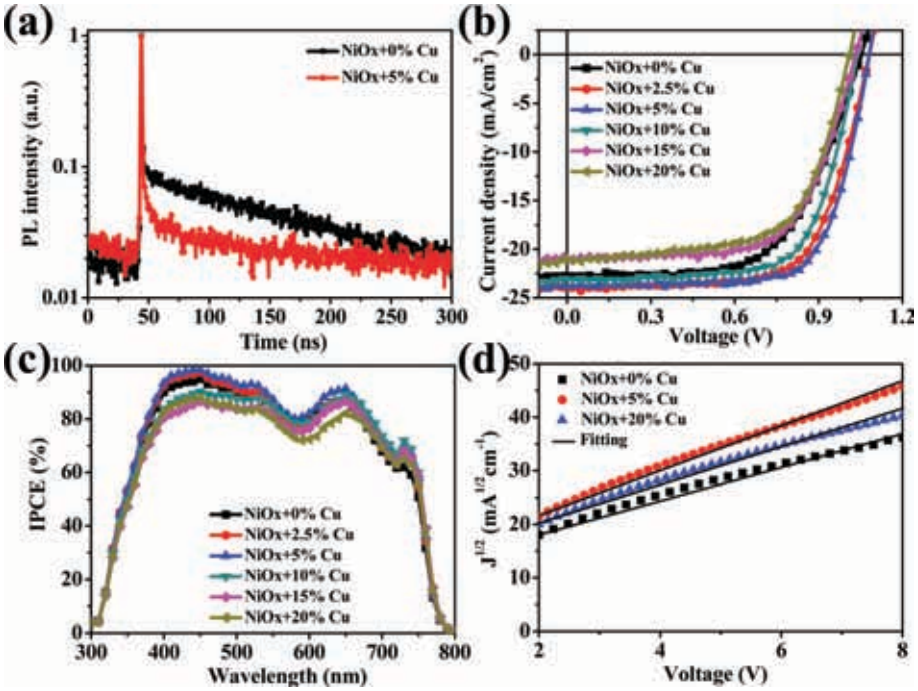

Fig. 3 (a) PL decay curves of the devices with the structure of ITO/NiO_x or 5% Cu doped NiO_x/$CH_3NH_3PbI_{3-x}Cl_x$. (b) The *J*–*V* curves of devices with different doping concentrations of Cu in NiO_x film under AM 1.5 light illumination. (c) The IPCE spectra of the corresponding devices. (d) $J^{1/2}$–*V* curves of the hole-only devices with the structure of ITO/NiO_x (0%, 5% and 20% of Cu doping)/$CH_3NH_3PbI_{3-x}Cl_x$/Au.

Cu $2p_{3/2}$ and Cu $2p_{1/2}$, respectively, assigned to the Cu^+.[30,31] The shakeup satellites between 932.5 eV and 952.6 eV are assigned to the presence of Cu^{2+}.[32] To test the positive contribution of Cu in NiO_x, transient PL signals were measured on the structure of ITO/NiO_x/$CH_3NH_3PbI_{3-x}Cl_x$ and ITO/5% Cu–NiO_x/$CH_3NH_3PbI_{3-x}Cl_x$. As shown in Fig. 3a, the existence of Cu in NiO_x boosts the PL signal decay for the corresponding film, thus indicating a faster hole transport process at the interface of 5% Cu–NiO_x and $CH_3NH_3PbI_{3-x}Cl_x$ in comparison with the counterpart without doping. Using the standard bi-exponential model, the lifetime of the curves was obtained as 6.3 ns and 1.4 ns, respectively. Fig. S10 (ESI†) shows the transmission spectra of the NiO_x film doped with different amounts of Cu. Considering that both Cu_2O and CuO have smaller bandgaps than that of NiO_x, it is expected that the increasing amount of Cu enhances the absorption capability of the corresponding films. The Tauc plots shown in Fig. S11 (ESI†) demonstrate that CuO_x is able to cause a redshift of the optical bandgap values of the composite films.

Fig. 3b shows the *J*–*V* curves of the devices with the NiO_x films doped with different amounts of Cu. These devices had been already optimized with modifications using 2 mg mL^{-1} ZrAcac solution and the according PCE statistical values are given in Fig. S12 (ESI†) and Table 2. As the doping amount of Cu was tuned from 0% to 5%, the devices presented a prominent increase in J_{sc}, V_{oc}, FF, and thus, PCE. The related best device in Table 2 (5% Cu doped) exhibited a PCE of 18.6%. A further increase of Cu in the film would cause the device performance to deteriorate. The IPCE spectra of these devices are given in Fig. 3c and the values exhibit the same varying tendency of the doping amount of Cu in NiO_x as is the case in J_{sc} and PCE (With doping amount of Cu increasing from 0% to 5%, IPCE value increases and further increment of doping amount drops the IPCE value.). The photocurrent values obtained by integrating the spectra are shown in Fig. S13 (ESI†) and these values are in approximate agreement with the J_{sc} given by the *J*–*V* curves.

Table 2 The photovoltaic performance of the perovskite solar cells shown in Fig. 3b

Samples	J_{sc} (mA cm^{-2})	V_{oc} (V)	FF (%)	PCE (%)
0% Cu	22.84 ± 0.32	1.06 ± 0.01	59.68 ± 2.79	14.47 ± 0.83
2.5% Cu	23.18 ± 0.43	1.09 ± 0.00	65.36 ± 1.64	16.55 ± 0.37
5% Cu	23.53 ± 0.32	1.10 ± 0.01	70.04 ± 1.47	18.05 ± 0.58
10% Cu	23.16 ± 0.27	1.05 ± 0.00	66.02 ± 1.16	16.04 ± 0.18
15% Cu	21.24 ± 0.18	1.03 ± 0.01	66.14 ± 2.79	14.41 ± 0.71
20% Cu	20.55 ± 0.40	1.02 ± 0.01	66.16 ± 1.92	13.79 ± 0.14

To further investigate the influence of the Cu doping in the NiO_x film on the hole transport of the devices, hole-only devices based on the structures of ITO/NiO_x (0%, 5% and 20% of Cu doping)/$CH_3NH_3PbI_{3-x}Cl_x$/gold were fabricated. The relevant $J^{1/2}$ *versus V* curves are given in Fig. 3d. The curves could be described by the following equation:[1]

$$J_D = \frac{9\mu\varepsilon\varepsilon_0 v^2}{8l^3} \quad (2)$$

where J_D is the dark current, μ is the hole mobility, ε is the relative dielectric constant of $CH_3NH_3PbI_{3-x}Cl_x$ ($\varepsilon = 28.8$),[33] ε_0 is the vacuum permittivity, v is applied voltage and L is the thickness of the active layer. A larger slope of the curve of $J^{1/2}$ *versus V* definitely results in a higher value of hole mobility. The fitted values are given in Table S3 (ESI†), where it could be

concluded that the device with 5% Cu doped NiO_x film exhibits the highest mobility of holes, among the devices used in this research. More detailed *J–V* curves in a large voltage range are provided in Fig. S14 (ESI†). In addition, the doping optimized device also presents a lower density of hole-trapping states when compared with other devices (Fig. S15 and Table S4; ESI†). Fig. S16 (ESI†) displays the impedance spectra of the devices using Cu doped NiO_x as the hole transport layer and illustrates that the device with 5% Cu doped NiO_x film shows an obvious superiority in the capability of its hole transport (Table S5; ESI†). To get more information on the positive contribution of Cu doping of NiO_x film, the UPS spectra were measured. As shown in Fig. 4, the Fermi level and valence band positions *versus* vacuum level could be obtained as 4.59 and 5.43 eV, 4.58 and 5.51 eV, 4.56 and 5.37 eV for the NiO_x, 5% Cu doped NiO_x and 20% Cu doped NiO_x film, respectively. An appropriate amount of Cu doping (*e.g.*, 5%) causes a slightly downward shift of valence band position, and this is helpful for collecting the photogenerated holes in the perovskite film with a low energy loss, because of the reduced distance between the valence band positions of 5% Cu–NiO_x and perovskite materials. Overloading of Cu in the film would make the NiO_x film show some features of CuO or Cu_2O. Because both the Cu related oxides have a valence band position that is above that of NiO_x,[34] it is understandable that the valance band position of the composite would be shifted upward by the overloading of Cu and the capability of the hole conducting of the film is worsened by the increase of energy loss for hole transport at the interface of $NiO_x/CH_3NH_3PbI_{3-x}Cl_x$. In addition, the large doping amount of Cu (*e.g.*, 20%) would increase the density of defects and hole traps in the NiO_x and the interface (Table S4; ESI†). These are detrimental for the device performance, particularly for the V_{oc}, FF and hole mobility.

Considering that the NiO_x annealing process at 340 °C would cause deterioration in the conductivity of the ITO substrate, a high-conductive FTO glass was used to further improve the PCE of the devices. The advantage of the used FTO substrate is discussed in Section S2 of the ESI.† As shown in Fig. 5a, before annealing the FTO substrates exhibit a smaller resistance than the ITO substrates (FTO resistance: 8.5 Ω sq^{-1}; ITO resistance: 12.8 Ω sq^{-1}). After annealing, however, the resistance of the ITO substrate increases sharply from 12.8 Ω sq^{-1} to 53.4 Ω sq^{-1} whereas FTO only presents a small change of resistance from 8.5 Ω sq^{-1} to 10.3 Ω sq^{-1}. This result shows the main advantage of using the FTO glass, because the annealing process does not obviously change the transmission capability and work function of both ITO and FTO substrates (Fig. S17; ESI†). Fig. 5b shows the *J–V* curves of the FTO-based devices fabricated by using the optimized conditions of Cu–NiO_x and ZrAcac. Excitingly, the FTO device delivers a much improved PCE, compared with the ITO device, particularly in the aspect of FF. The optimized PCE is about 20.5%, which is almost the highest value obtained for the $CH_3NH_3PbI_{3-x}Cl_x$-based devices. The performance parameters with statistical values are given in Table 3. The improvement in FF is mainly attributed to the satisfactory conductivity of the FTO substrates and this was also concluded from the reduction of charge transport resistance of the device as shown by the impedance spectra given in Fig. 5c. The detailed fitting parameters for charge transport are given in Table S6 (ESI†) and a discussion on all the fitted parameters (shown in Fig. 2f, Fig. S16 (ESI†) and Fig. 5c) corresponding to the device performance is given in Section S3 of the ESI.† The forward and reverse scans for the FTO-based devices are given in Fig. S18 (ESI†). In the reverse scan, FF and V_{oc} only present a slight decrease and the PCE is 20.1%. Such slight variation indicates that the relevant device shows a good capability against hysteresis.

Collectively, a systematic approach to optimize the performance of perovskite solar cells has been provided. The key factors governing the extraction of the charge carriers are the bandgap alignment across the whole device and the conducting nature of each component. Fig. 5d displays the bandgap alignment of the device. The bandgap structures of $CH_3NH_3PbI_{3-x}Cl_x$ and $PC_{61}BM$ were obtained from the relevant UPS spectra and absorption spectra (Fig. S3 and S19; ESI†). The Al cathode is for collecting the electrons generated in the active layer. Because it has been systematically reported in a previous paper that lowering the work function of the cathode appropriately is beneficial for the improvement of device performance,[35] it was not focused on in this research. A purposely inserted proper thickness of ZrAcac is beneficial for promoting the electron transport from $PC_{61}BM$ to Al by reducing the corresponding transport resistance and trapping states. The formation of interfacial dipole induced by a ZrAcac thin layer at $PC_{61}BM$/Al is responsible for such an improvement because of the formation

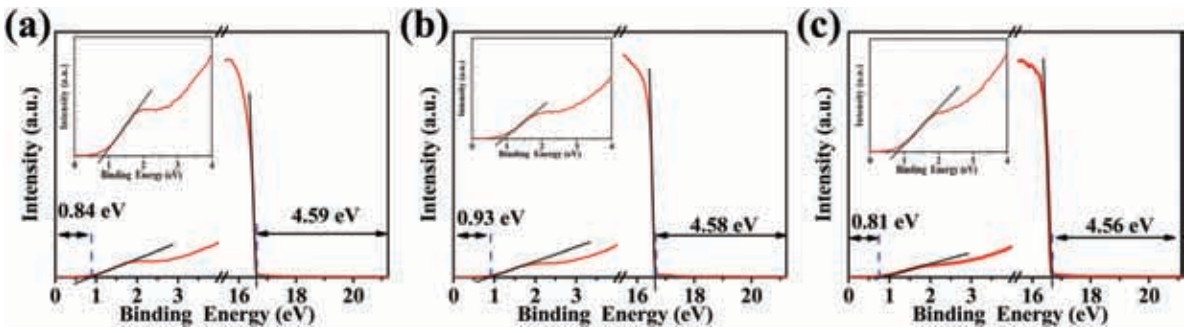

Fig. 4 The UPS of a series of Cu doped NiO_x film, the inset zooms in on the low binding energy region. (a) NiO_x (b) NiO_x + 5% Cu (c) NiO_x + 20% Cu.

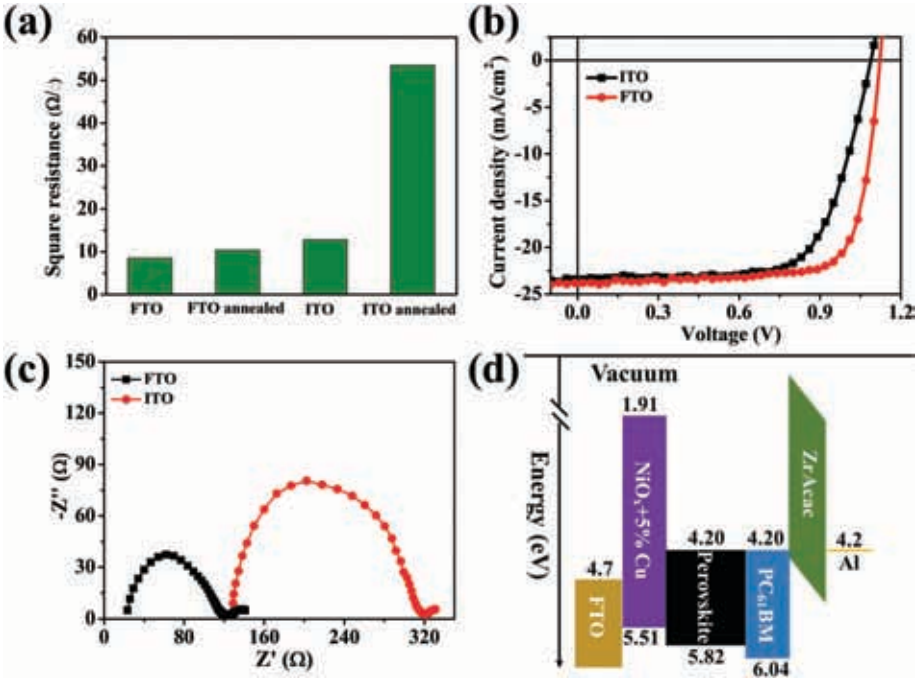

Fig. 5 (a) The variation of square resistance for the substrates before and after annealing. (b) The J–V curves of devices with different substrates under AM 1.5. (c) Nyquist plots of the devices measured in dark at $V \approx V_{oc}$. (d) Schematic drawing of the band energy diagrams for the inverted structured perovskite solar cell.

Table 3 The photovoltaic performance of perovskite solar cells in Fig. 5b

Samples	J_{sc} [mA cm^{-2}]	V_{oc} [V]	FF [%]	PCE [%]
FTO	23.07 ± 0.42	1.12 ± 0.01	77.06 ± 0.55	20.14 ± 0.33
ITO	23.53 ± 0.32	1.10 ± 0.01	70.04 ± 1.47	18.05 ± 0.58

of (quasi) Ohmic contact between $PC_{61}BM$ and Al from the molecule modification.[19,36,37] The quality of $PC_{61}BM$ as the electron transport layer is also of importance and the corresponding electron conducting property could be ameliorated by improving the crystallinity using ethanol treatment. This is similar to the case in polymer solar cells and is the additional bonus from spin-coating the ZrAcac in ethanol solution.[21] Generally, the improvement in electron transport of the device would directly enhance the FF of the devices. Factors limiting FF are widely discussed as a field dependent competition between non-geminate recombination and charge extraction, with trap states and departure from diode ideality playing important roles.[38] As shown in Fig. S20 (ESI†), the contact between $PC_{61}BM$/ZrAcac/Al usually represents an efficient electron extraction. The charge transport resistance at the interfaces could be significantly reduced by the presence of ZrAcac of a suitable thickness (as discussed in Section S2; ESI†). Thus the enhanced electron extraction and depressed recombination make the tradeoff positive to the FF increase. In addition, J_{sc} is also increased by the improvement of electron transport and reduction of the trap state, attributed to the depressed electron loss in the transport. However, V_{oc} is only improved slightly because of the fact that V_{oc} is mainly determined by the band gap of the perovskite material and the alignment of the energy level.[35,39] The slightly improved V_{oc} could be attributed to the modification effect of ZrAcac, because it moves the surface potential of Al positively and would be helpful for the Al electrode to collect the electron with a relatively low energy loss (Fig. S21; ESI†).

The Cl doped $CH_3NH_3PbI_3$ film shows a relatively larger bandgap than the intrinsic material and the 0.04 eV widening in bandgap results in a 0.1 V enchantment in V_{oc} (Fig. S22; ESI†). This indicates that a large bandgap is energetically favorable for realizing a large V_{oc}.[40] The 0.1 V improvement in V_{oc} particularly demonstrates that the Cl-based perovskite material exhibits a superior capability for converting the solar energy to charge carriers and transporting them to the electrodes with a low energy loss. In comparison with the band structure of $CH_3NH_3PbI_3$,[35] both the positions of valence band and conduction band of $CH_3NH_3PbI_{3-x}Cl_x$ present a downwards movement *versus* vacuum energy level. This is favorable for the NiO_x layer to collect the photogenerated holes and $PC_{61}BM$ layer to collect the electrons with low energy loss because of the match of these band energy positions. In addition, with the same device configuration, the Cl-based device presents an improvement in both electron and hole mobilities (Fig. S23; ESI†). This is responsible for the remarkable improvement in FF for the Cl doped devices. The J_{sc} of the two devices is similar. Although the improvement in electron and hole mobilities could enhance the J_{sc} of the Cl-based device by reducing the charge recombination, the enlarged band gap of the $CH_3NH_3PbI_{3-x}Cl_x$ would deteriorate the generation of photo-excited charge carriers. More detailed discussion on the Cl incorporation to the perovskite is given in Section S1 of the ESI.† For the hole transport layer, for the first time, it has been demonstrated that the proper amount doping of Cu in the NiO_x

film is of great benefit in boosting the hole transport to the electrode with a low resistance and trap states, and thus a high transport mobility. This effect results from the reduced distance of the valence band positions between optimized Cu–NiO_x film and the Cl-based perovskite material, which is energetically favorable to reduce the energy loss of the hole transport at the interface. The reduced energy loss is relevant to the 0.05 V improvement in V_{oc} in comparison with the device without Cu doping. The enhancement in hole mobility and reduction in hole trap states are responsible for the improvement in FF and J_{sc}, and are similar to the discussion on electron transport. In addition, the thermally stable FTO substrate with a high conductivity and transmission is also of importance in realizing a high PCE. The high conductivity of the substrate is of significance for reducing the recombination of the charge carriers, and is particularly beneficial for improving FF.

Conclusions

In summary, a systematic approach was used to optimize the performance of PSCs, using a Cl-doped $CH_3NH_3PbI_3$ active layer, modifying the electron capture using a ZrAcac buffer layer, boosting the hole transport by doping the NiO_x film with Cu and adopting the use of a FTO substrate with a high thermal stability and conductivity. Consequently, a PCE about 20.5% has been realized and such a value is almost the highest one for the $CH_3NH_3PbI_{3-x}Cl_x$-based photovoltaic devices. Insights on how to manage the extraction of charge carriers efficiently are illustrated using multiple techniques and guidelines on how to construct highly efficient perovskite solar cells are given in this paper.

Experimental

Materials and solution preparation

Methylammonium iodide (MAI; >99.5%) and PbI_2 (>99.99%) were purchased from Xi'an Polymer Light Technology Corp. $PC_{61}BM$ (>99.9%) and anhydrous *N,N*-dimethylformamide (DMF, 99.8%) were purchased from Sigma-Aldrich. Nickel acetate tetrahydrate ($Ni(ac)_2$; $Ni(CH_3COO)_2{\cdot}4H_2O$) and cupric acetate monohydrate ($Cu(ac)_2$; $Cu(CH_3COO)_2{\cdot}H_2O$) were obtained from Sinopharm Chemical Reagent Co., Ltd. Zirconium(IV) acetylacetonate (ZrAcac; $ZrC_{20}H_{28}O_8$) was provided by Alfa Aesar. All the solvents were purchased from the Beijing Chemical Works. Unless otherwise stated, all the chemicals were used as received.

MAI, PbI_2 and $PbCl_2$ were mixed in the ratio of (1 : 0.9 : 0.1) in anhydrous DMF. The concentration of the perovskite precursor was 1.2 M. The mixture was then stirred overnight at 60 °C under a nitrogen atmosphere. The final solution of the perovskite precursor was stored in a glove box, and filtered using 0.45 μm PTFE filters before use. $Ni(ac)_2$ and $Cu(ac)_2$ were dissolved in 0.1 M anhydrous ethanol. Cu doped NiO_x films were prepared by varying the volume ratio of the solution (Ni : Cu, 100 : 0, 97.5 : 2.5, 95 : 5, 90 : 10, 85 : 15, 80 : 20). ZrAcac was dissolved in anhydrous ethanol at a series of concentrations from 0 to 4 mg mL^{-1}.

Device fabrication

Devices were fabricated on prepatterned ITO (FTO) substrates cleaned using ultrasonication in deionized water, acetone, and isopropanol for 20 min each and then dried under a nitrogen flow. The mixed NiO_x solution was spin-coated onto the ITO (FTO) surface at 3000 rpm for 40 s and then annealed at 340 °C for 60 min in an ambient atmosphere. To deposit perovskite films, these substrates were transferred into an inert glove box under a nitrogen atmosphere (H_2O and O_2 <1 ppm). The perovskite solution was dropped onto the center of the substrates. Then substrates were spun at 6000 rpm for 30 s, and after 5 s anhydrous toluene was quickly dropped onto the center of substrate. The instant color change of the films from yellow to brown was observed upon dropping toluene solvent. The resulting dark brown films were dried at 100 °C for 10 min. Next, $PC_{61}BM$ (20 mg mL^{-1}) in chlorobenzene solution was coated onto the perovskite layer at 1000 rpm for 60 s. The next step was spin-coating the ZrAcac and the solution was coated onto the $PC_{61}BM$ layer at 2000 rpm for 60 s. Finally, 100 nm of Al was deposited using thermal evaporation under a high vacuum.

Characterization

The absorbance spectrum was measured on a TU-1950 ultraviolet-visible spectrophotometer (Persee, Beijing) in transmission mode. UPS data were obtained using an Axis Ultra DLD (Kratos Analytical). XPS data were obtained using an ESCALAB 250Xi (Thermo Fisher Scientific). The cross-sectional SEM image of the device structure was measured using a JSM-7401F (Jeol). The current density–voltage (*J–V*) characteristics were obtained using a 2450 source measure unit (Keithley) under AM 1.5 illumination with an intensity of 100 mW cm^{-1}. IPCE measurements were performed using a QEPVSI-b Measurement System (Newport Corporation). Impedance spectroscopy measurement was performed using a CHI660E electrochemical workstation (CH Instruments) under dark conditions, with an oscillating voltage of 10 mV and frequency scanning range of 100 Hz to 1 M Hz. The transient PL measurements were performed using a F900 time-correlated single photon counting system (Edinburgh Instruments) and the samples were excited using a pulsed laser with the wavelength of 485 nm. The XRD spectra were measured using a V2500 (Rigaku) X-ray diffractometer.

Conflicts of interest

There are no conflicts to declare.

Acknowledgements

This work was mostly supported by the National Basic Research Program of China (Grant No. 2014CB643503), the National Key Research and Development Program of China (Grant No. 2017YFA0206600), the Key Research Program of Frontier Science, Chinese Academy of Sciences (Grant No. QYZDB-SSW-SLH006), the National Natural Science Foundation of China (Contract No. 61674141, 61504134 and 21503209), the Beijing Natural Science

Foundation (2162042), the European Research Council (ThreeDsurface, 240144 and HiNaPc, 737616), the German Federal Ministry of Education and Research (BMBF, ZIK-3DNanoDevice, 03Z1MN11), and the German Research Foundation (DFG, LE 2249_4-1). ZW appreciates the support from Hundred Talents Program (Chinese Academy of Sciences).

Notes and references

1 Q. Dong, Y. Fang, Y. Shao, P. Mulligan, J. Qiu, L. Cao and J. Huang, *Science*, 2015, **347**, 967–970.
2 J. P. Correa-Baena, A. Abate, M. Saliba, W. Tress, T. J. Jacobsson, M. Gratzel and A. Hagfeldt, *Energy Environ. Sci.*, 2017, **10**, 710–727.
3 M. Saliba, T. Matsui, J. Y. Seo, K. Domanski, J. P. Correa-Baena, M. K. Nazeeruddin, S. M. Zakeeruddin, W. Tress, A. Abate, A. Hagfeldt and M. Gratzel, *Energy Environ. Sci.*, 2016, **9**, 1989–1997.
4 H. Tan, A. Jain, O. Voznyy, X. Lan, F. P. Garcia de Arquer, J. Z. Fan, R. Quintero-Bermudez, M. Yuan, B. Zhang, Y. Zhao, F. Fan, P. Li, L. N. Quan, Y. Zhao, Z. H. Lu, Z. Yang, S. Hoogland and E. H. Sargent, *Science*, 2017, **355**, 722–726.
5 W. S. Yang, J. H. Noh, N. J. Jeon, Y. C. Kim, S. Ryu, J. Seo and S. I. Seok, *Science*, 2015, **348**, 1234–1237.
6 W. Nie, H. Tsai, R. Asadpour, J. C. Blancon, A. J. Neukirch, G. Gupta, J. J. Crochet, M. Chhowalla, S. Tretiak, M. A. Alam, H. L. Wang and A. D. Mohite, *Science*, 2015, **347**, 522–525.
7 H. L. Kim, K.-G. Lee and T.-W. Lee, *Energy Environ. Sci.*, 2016, **9**, 12–30.
8 Y. Shao, Y. Yuan and J. Huang, *Nat. Energy*, 2016, **1**, 15001.
9 Y. Li, S. Ye, W. Sun, W. Yan, Y. Li, Z. Bian, Z. Liu, S. Wang and C. Huang, *J. Mater. Chem. A*, 2015, **3**, 18389–18394.
10 D. Liu and T. L. Kelly, *Nat. Photonics*, 2014, **8**, 133–138.
11 M. M. Lee, J. Teuscher, T. Miyasaka, T. N. Murakami and H. J. Snaith, *Science*, 2012, **338**, 643–647.
12 P.-W. Liang, C.-Y. Liao, C.-C. Chueh, F. Zuo, S. T. Williams, X.-K. Xin, J. Lin and A. K. Y. Jen, *Adv. Mater.*, 2014, **26**, 3748–3754.
13 Z. He, C. Zhong, S. Su, M. Xu, H. Wu and Y. Cao, *Nat. Photonics*, 2012, **6**, 591–595.
14 J.-Y. Jeng, Y.-F. Chiang, M.-H. Lee, S.-R. Peng, T.-F. Guo, P. Chen and T.-C. Wen, *Adv. Mater.*, 2013, **25**, 3727–3732.
15 N. J. Jeon, J. H. Noh, Y. C. Kim, W. S. Yang, S. Ryu and S. Il Seol, *Nat. Mater.*, 2014, **13**, 897–903.
16 Q. Jiang, L. Zhang, H. Wang, X. Yang, J. Meng, H. Liu, Z. Yin, J. Wu, X. Zhang and J. You, *Nat. Energy*, 2016, **1**, 16177.
17 F. Jiang, Y. Rong, H. Liu, T. Liu, L. Mao, W. Meng, F. Qin, Y. Jiang, B. Luo, S. Xiong, J. Tong, Y. Liu, Z. Li, H. Han and Y. Zhou, *Adv. Funct. Mater.*, 2016, **26**, 8119–8127.
18 Y. C. Kim, N. J. Jeon, J. H. Noh, W. S. Yang, J. Seo, J. S. Yun, A. Ho-Baillie, S. Huang, M. A. Green, J. Seidel, T. K. Ahn and S. I. Seok, *Adv. Energy Mater.*, 2016, **6**, 1502104.
19 W. B. Yan, S. Y. Ye, Y. L. Li, W. H. Sun, H. X. Rao, Z. W. Liu, Z. Q. Bian and C. Huang, *Adv. Energy Mater.*, 2016, **6**, 1600474.
20 J. W. Li, Q. S. Dong, N. Li and L. D. Wang, *Adv. Energy Mater.*, 2017, **7**, 1602922.
21 S. Lu, K. Liu, D. Chi, S. Yue, Y. Li, Y. Kou, X. Lin, Z. Wang, S. Qu and Z. Wang, *J. Power Sources*, 2015, **300**, 238–244.
22 S. Guo, B. Cao, W. Wang, J. F. Moulin and P. Muller-Buschbaum, *ACS Appl. Mater. Interfaces*, 2015, **7**, 4641–4649.
23 Q. Dong, Y. Fang, Y. Shao, P. Mulligan, J. Qiu, L. Cao and J. Huang, *Science*, 2015, **347**, 967–970.
24 D. Yang, R. Yang, X. Ren, X. Zhu, Z. Yang, C. Li and S. F. Liu, *Adv. Mater.*, 2016, **28**, 5206–5213.
25 J. H. Kim, P. W. Liang, S. T. Williams, N. Cho, C. C. Chueh, M. S. Glaz, D. S. Ginger and A. K. Jen, *Adv. Mater.*, 2015, **27**, 695–701.
26 J. W. Jung, C. C. Chueh and A. K. Jen, *Adv. Mater.*, 2015, **27**, 7874–7880.
27 H. Yan, D. Zhang, J. Xu, Y. Lu, Y. Liu, K. Qiu, Y. Zhang and Y. Luo, *Nanoscale Res. Lett.*, 2014, **9**, 424.
28 M. A. Abbasi, Z. H. Ibupoto, M. Hussain, Y. Khan, A. Khan, O. Nur and M. Willander, *Sensors*, 2012, **12**, 15424–15437.
29 C. Guan, Y. Wang, Y. Hu, J. Liu, K. H. Ho, W. Zhao, Z. Fan, Z. Shen, H. Zhang and J. Wang, *J. Mater. Chem. A*, 2015, **3**, 23283–23288.
30 P. Wang, Y. H. Ng and R. Amal, *Nanoscale*, 2013, **5**, 2952–2958.
31 A. A. Dubale, W.-N. Su, A. G. Tamirat, C.-J. Pan, B. A. Aragaw, H.-M. Chen, C.-H. Chen and B.-J. Hwang, *J. Mater. Chem. A*, 2014, **2**, 18383–18397.
32 Z. Zhang and P. Wang, *J. Mater. Chem.*, 2012, **22**, 2456–2464.
33 D. Yang, X. Zhou, R. X. Yang, Z. Yang, W. Yu, X. L. Wang, C. Li, S. Z. Liu and R. P. H. Chang, *Energy Environ. Sci.*, 2016, **9**, 3071–3078.
34 M. T. Greiner, M. G. Helander, W. M. Tang, Z. B. Wang, J. Qiu and Z. H. Lu, *Nat. Mater.*, 2011, **11**, 76–81.
35 S. Yue, S. Lu, K. Ren, K. Liu, M. Azam, D. Cao, Z. Wang, Y. Lei, S. Qu and Z. Wang, *Small*, 2017, **13**, 1700007.
36 S.-Y. Chang, Y.-C. Lin, P. Sun, Y.-T. Hsieh, L. Meng, S.-H. Bae, Y.-W. Su, W. Huang, C. Zhu, G. Li, K.-H. Wei and Y. Yang, *Solar RRL*, 2017, **1**, 1700139.
37 W. Chen, L. Xu, X. Feng, J. Jie and Z. He, *Adv. Mater.*, 2017, **29**, 1603923.
38 D. Bartesaghi, C. Perez Idel, J. Kniepert, S. Roland, M. Turbiez, D. Neher and L. J. Koster, *Nat. Commun.*, 2015, **6**, 7083.
39 A. Guerrero, L. F. Marchesi, P. P. Boix, S. Ruiz-Raga, T. Ripolles-Sanchis, G. Garcia-Belmonte and J. Bisquert, *ACS Nano*, 2012, **6**, 3453–3460.
40 Q. Xue, Y. Bai, M. Liu, R. Xia, Z. Hu, Z. Chen, X.-F. Jiang, F. Huang, S. Yang, Y. Matsuo, H.-L. Yip and Y. Cao, *Adv. Energy Mater.*, 2017, **7**, 1602333.

